

Prediction of Multiple Dry-Wet Transition Pathways with a Mesoscale Variational Approach

Shenggao Zhou,¹ Yanan Zhang^{a,2} Li-Tien Cheng,³ and Bo Li^{a,3}

¹*School of Mathematical Sciences and MOE-LSC,*

Shanghai Jiao Tong University, Shanghai, 200240, China

²*School of Mathematical Sciences, Soochow University, Suzhou, 215006, China*

³*Department of Mathematics, University of California,*

San Diego, La Jolla, California 92093-0112, U.S.A.

(Dated: September 15, 2021)

^a Authors to whom correspondance should be addressed: ynzhang@suda.edu.cn and bli@math.ucsd.edu

ABSTRACT

Water fluctuates in a hydrophobic confinement, forming multiple dry and wet hydration states through evaporation and condensation. Transitions between such states are critical to both thermodynamics and kinetics of solute molecular processes such as protein folding and protein-ligand binding and unbinding. To efficiently predict such dry-wet transition paths, we develop a hybrid approach that combines a variational implicit solvation model, a generalized string method for minimum free-energy paths, and the level-set numerical implementation. This approach is applied to three molecular systems: two hydrophobic plates, a carbon nanotube, and a synthetic host molecule Cucurbit[7]uril. Without explicit description of individual water molecules, our mesoscale approach captures well multiple dry and wet hydration states, multiple dry-wet transition paths such as those geometrically symmetric and asymmetric paths, and transition states, providing activation energy barriers between different states. Further analysis shows that energy barriers depend on mesoscopic lengths such as the separation distance between the two plates and the cross-section diameter of the nanotube, and that the electrostatic interactions strongly influence the dry-wet transitions. With the inclusion of solute atomic motion, general collective variables as reaction coordinates, and the finite-temperature string method, together

with an improved treatment of continuum electrostatics, our approach can be further developed to sample an ensemble of transition paths, providing more accurate predictions of the transition kinetics.

I. INTRODUCTION

Water plays a crucial role in many biomolecular processes, such as protein folding, protein-ligand binding and unbinding, and ion permeation through transmembrane channels.¹⁻⁴ In a hydrophobic confinement, such as a concave pocket on a protein surface and a transmembrane protein channel, water molecules are metastable, as they are unable to form a stable hydrogen-bond network. Because of thermal fluctuations, water molecules constantly fill and condensate in the confinement and leave or evaporate from the confinement, undergoing wetting (i.e., dry-to-wet) and dewetting (i.e., wet-to-dry) transitions. Such transitions mediate biomolecular processes.⁵⁻⁷ For instance, hydrophobic dewetting provides the driving force for protein folding.^{1,8,9} Dry and wet transitions are a precursor of the binding and unbinding of a ligand to a hydrophobic pocket of a receptor protein, and significantly influence the kinetics of such processes.^{3,10-13} Dewetting in a hydrophobic nanopore also causes considerably high energy barriers to ion permeation.^{2,4}

While water is an active player in many biological processes, efficient modeling of water is rather challenging, due to a large number of water molecules in an underlying system and the multiscale nature of molecular hydration. Explicit-water molecular dynamics (MD) simulations have been a powerful approach for capturing the detailed solvent effects. However, such simulations are limited to systems of relatively small sizes and events of relatively short timescales. Barrier-crossing rare events such as wetting and dewetting transitions, often with high energy barriers, can involve much longer timescales that cause MD simulations to be much too expensive.

In this work, we develop a mesoscale hybrid modeling and computational approach to study quantitatively the wetting and dewetting transitions in molecular hydration. We describe a (meta)stable equilibrium hydration state by a solute-solvent interface. It is obtained by minimizing a solvation free-energy functional of all possible surfaces that enclose all the solute atoms that are assumed to be fixed. The free energy consists of the solute-solvent interfacial energy, the solute-solvent van der Waals (vdW) free energy accounting for the

short-ranged excluded-volume effect and the long-ranged attraction, and the electrostatic interaction energy.^{14–17} For efficiency, we use the Coulomb-field approximation (CFA) of the electrostatic interaction.^{16–23} Numerically, the minimization is carried out iteratively in the direction of steepest descent by the level-set method. With different initial interfaces, our method predicts different dry and wet solvation states.^{16,17,22–25} Once a dry and a wet state are found, we then use the string method,^{13,26–30} generalized to surfaces rather than points in a Euclidean space, to find minimum energy paths, i.e., the transition paths, connecting these hydration states. Transition states (i.e., saddle points) along such paths and energy barriers for the dry-to-wet and wet-to-dry transitions can be further found.

We apply our approach to study quantitatively the dry-wet transition pathways for three hydration systems: two parallel hydrophobic plates, a carbon nanotube, and a synthetic host molecule Cucurbit[7]uril (CB[7]). The last two systems are of practical interest in materials and drug development. From our extensive computations and analysis, we see that it is common to have multiple transition paths, such as geometrically symmetric and geometrically asymmetric ones. Moreover, the transitions depend sensitively on the different length scales of an underlying system. and electrostatic interactions can influence significantly the stability of transition paths. It is generally true that the activation energy barriers for the wetting and dewetting transitions can be quite different. Our results agree well with existing MD simulations.

Previously, our level-set implicit solvation approach captured different dry and wet states for complex molecular systems.^{16,17,31} Our stochastic level-set method for two parallel hydrophobic plates successfully captured the dewetting transition, but not the wetting transition under similar simulation times.³² This seems to be reasonable, as our current study clearly shows that the energy barrier for the wetting transition is in fact much higher than that of the dewetting transition. Compared with our initial work for a model system,¹³ our results here are much more detailed and quantitative, particularly on the effect of length scales and electrostatic interactions to both wetting and dewetting transition paths, and the energy barriers in such transitions.

In Section II, we describe briefly our variational solvation theory, the numerical level-set method, and the string method generalized for surfaces. In Section III, we present our computational results of multiple transition paths and energy barriers, and the related analysis. In Section IV, we draw conclusions. Finally, Section V (APPENDIX) collects some

algorithms of our generalized string methods.

II. THEORY AND METHODS

A. A Variational Implicit Solvation Model

We consider a solute molecule immersed in an aqueous solvent. The spatial solvation region is determined by a solute-solvent interface Γ that separates the solute region Ω_m (m for molecule) from the solvent region Ω_w (w for water), with the dielectric coefficient ε_m and ε_w , respectively; cf. Fig. 1. The position vectors and partial charges of all the solute atoms (assumed to be inside the solute region Ω_m) are denoted by $\mathbf{x}_1, \dots, \mathbf{x}_N$ and Q_1, \dots, Q_N , respectively.

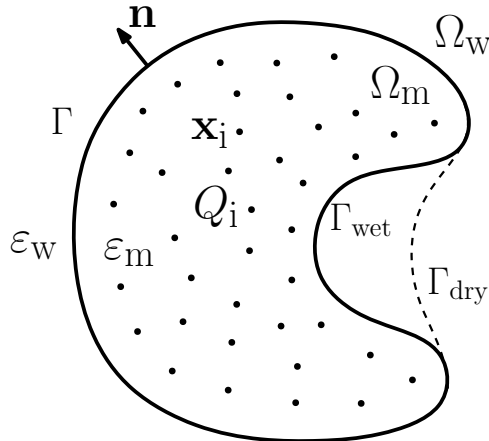


FIG. 1: A schematic view of a solvation system with an implicit solvent. Notations: Ω_m and Ω_w are solute and solvent regions; ε_m and ε_w are the corresponding dielectric coefficients; $\mathbf{x}_1, \dots, \mathbf{x}_N$ and Q_1, \dots, Q_N are the position vectors and partial charges of solute atoms; Γ is a solute-solvent interface or dielectric boundary; and \mathbf{n} is the unit normal at the interface Γ . If the interface Γ is found to be Γ_{wet} or Γ_{dry} , then the concave pocket region on the solute surface is wet or dry, respectively.

We introduce the solvation free energy $G[\Gamma]$ of a solute-solvent interface Γ :^{14,15,17,23}

$$G[\Gamma] = \int_{\Gamma} \gamma_0(1 - 2\tau H) dS + \rho_w \sum_{i=1}^N \int_{\Omega_w} U_i(|\mathbf{x} - \mathbf{x}_i|) dV + G_{\text{elec}}[\Gamma], \quad (1)$$

$$G_{\text{elec}}[\Gamma] = \frac{1}{32\pi^2\varepsilon_0} \left(\frac{1}{\varepsilon_w} - \frac{1}{\varepsilon_m} \right) \int_{\Omega_w} \left| \sum_{i=1}^N \frac{Q_i(\mathbf{x} - \mathbf{x}_i)}{|\mathbf{x} - \mathbf{x}_i|^3} \right|^2 dV. \quad (2)$$

The first term in Eq. (1) is the solute-solvent interfacial energy, where γ_0 is a constant surface tension for a planar interface, τ is the curvature correction coefficient,³³ and H is the local mean curvature defined as the mean of principal curvatures. The second term in Eq. (1) describes the solute-solvent van der Waals (vdW) type dispersive interaction. The solvent here is treated implicitly, and such interaction energy is then given by the integral over the solvent region. The constant ρ_w is the bulk solvent number density. For each i , the potential U_i is a Lennard-Jones (LJ) potential given by

$$U_i(r) = 4\varepsilon_i \left[\left(\frac{\sigma_i}{r} \right)^{12} - \left(\frac{\sigma_i}{r} \right)^6 \right], \quad (3)$$

where the parameters ε_i of energy and σ_i of length can be different for each i . The last term $G_{\text{elec}}[\Gamma]$ in Eq. (1) is the electrostatic interaction energy. It is given by the Coulomb-field approximation (CFA) Eq. (2),^{16,18-20} where ε_0 is the vacuum permittivity.

Minimization of the free energy $G[\Gamma]$ among all the possible solute-solvent interfaces or dielectric boundaries Γ determines an optimal such interface Γ , representing a stable equilibrium solvation conformation. The minimum value $G[\Gamma]$ is an approximation of the corresponding solvation free energy. The free-energy minimization starts with an initial guess and proceeds with moving the interface Γ in the steepest descent direction. Only the normal component of this direction is needed in relaxing the interface. This normal component is exactly the normal force acting on the interface Γ , i.e., the negative variation of the free energy $G[\Gamma]$ with respect to the location change of Γ :^{16,17,24,25}

$$\begin{aligned} -\delta_{\Gamma}G[\Gamma](\mathbf{x}) = & -2\gamma_0[H(\mathbf{x}) - \tau K(\mathbf{x})] + \rho_w \sum_{i=1}^N U_i(|\mathbf{x} - \mathbf{x}_i|) \\ & + \frac{1}{32\pi^2\varepsilon_0} \left(\frac{1}{\varepsilon_w} - \frac{1}{\varepsilon_m} \right) \left| \sum_{i=1}^N \frac{Q_i(\mathbf{x} - \mathbf{x}_i)}{|\mathbf{x} - \mathbf{x}_i|^3} \right|^2 \quad \text{for } \mathbf{x} \in \Gamma, \end{aligned} \quad (4)$$

where $K(\mathbf{x})$ is the Gaussian curvature at \mathbf{x} . With different initial interfaces, the minimization can lead to different minimizers that are metastable equilibrium solvation states, often corresponding to different dry and wet states. With the steepest descent of the free energy $G[\Gamma]$, a tight initial interface that wraps up tightly all the solute atoms and a loose initial interface that is a large surface enclosing all the solute atoms can often lead to a wet state and a dry state, respectively.

We remark that the CFA does not include ionic charges and hence the screening effect. Nevertheless, it has been systematically tested that the CFA incorporated into our

variational model can in general capture different dry and wet solvation states, provide reasonably good estimates of the solvation free energy, and also predict the desolvation barrier qualitatively.^{16,17,21–23}

B. The Level-Set Numerical Implementation

Previously, we implemented a level-set method to minimize numerically the free-energy functional $G[\Gamma]$ defined in Eq. (1).^{16,17,24,25,31,34} Here, we only describe the method briefly to set notations. The key of the method is to represent the solute-solvent interface Γ at time t by a zero level set of a level-set function $\phi = \phi(\mathbf{x}, t)$, i.e., the points \mathbf{x} on the surface Γ at time t are exactly those satisfying $\phi(\mathbf{x}, t) = 0$. With such a representation, all the unit normal, mean curvature, and Gaussian curvature, can be explicitly expressed through the level set function. The steepest descent method for relaxing the free energy is realized by tracking the zero level set of the function $\phi(\mathbf{x}, t)$, which satisfies the level-set equation

$$\partial_t \phi + F_n |\nabla \phi| = 0, \quad (5)$$

where $F_n = -\delta_\Gamma G[\Gamma]$ is the normal component of the boundary force given by Eq. (4). Notice that the equation is only defined for $\mathbf{x} \in \Gamma$ so the force F_n needs to be extended to the entire computational box. Moreover, after a few steps of optimization, we reinitialize the level-set function by solving^{16,17,24,25}

$$\phi_t + \text{sign}(\phi_0)(|\nabla \phi| - 1) = 0, \quad (6)$$

where ϕ_0 is the level-set function before reinitialization and $\text{sign}(\phi_0)$ represents the sign of ϕ_0 .²⁵ Notice that the pseudo time t here is different from the one in the original level-set equation (5).

C. The String Method Generalized

We generalize the string method^{26,28,30} (both the simplified and climbing string methods) for points in a Euclidean space to that for surfaces or level-set functions. Such generalization was first made in our previous work.¹³ Here we describe briefly these generalized simplified and climbing string method coupled with our variational model and the level-set method,

with some variations. For instance, we include the CFA of the electrostatic interactions in our solvation model.

Let us fix all the solute atoms, and consider two stable equilibrium solvation states that are represented by the solute-solvent interfaces Γ_0 and Γ_1 with the corresponding level-set functions ϕ_0 and ϕ_1 , respectively. We first consider the simplified string method. We define a string or path that connects these two states to be a family of solute-solvent interfaces $\{\Gamma_\alpha\}_{\alpha \in [0,1]}$, or their corresponding level-set functions $\{\phi_\alpha\}_{\alpha \in [0,1]}$, that connect the two states Γ_0 and Γ_1 , or their level-set functions ϕ_0 and ϕ_1 . A minimum energy path (MEP) is a string that is orthogonal to the level surfaces of the solvation free-energy functional $G[\Gamma]$ defined in Eq. (1). The orthogonality is defined by the L^2 -inner product of the level-set functions. By the large deviation theory,³⁵ a MEP is the most probable transition path, in the sense that other paths have exponentially smaller transition probability. Within the level-set framework, we obtain a MEP by solving the equation for the level-set function $\phi_\alpha = \phi_\alpha(x, t)$:

$$\partial_t \phi_\alpha = -F_n(\phi_\alpha) |\nabla \phi_\alpha| + \lambda_\alpha \frac{\partial_\alpha \phi_\alpha}{\|\partial_\alpha \phi_\alpha\|} \quad \text{for } \alpha \in (0, 1), \quad (7)$$

to a steady state, starting from a given initial string $\{\phi_\alpha^{(0)}\}_{\alpha \in [0,1]}$ that connects ϕ_0 and ϕ_1 . Here, $F_n(\phi_\alpha) = -\delta_\Gamma G[\Gamma_\alpha]$ (cf. Eq. (4)), $\partial_\alpha \phi_\alpha / \|\partial_\alpha \phi_\alpha\|$ is the unit vector tangential to the string, λ_α is a Lagrange multiplier for enforcing the equal arc-length or energy weighted arc-length parameterization, and $\|\cdot\|$ denotes the $L^2(\Omega)$ -norm.

For an integer $M \geq 2$, we discretize the parameter α into $0 = \alpha_0 < \alpha_1 < \dots < \alpha_M < \alpha_{M+1} = 1$ and discretize the string into $M + 2$ images: $\phi_{\alpha_0}, \phi_{\alpha_1}, \dots, \phi_{\alpha_{M+1}}$. We also set the initial images to be

$$\phi_{\alpha_j}^{(0)} = \phi_0 + \alpha_j(\phi_1 - \phi_0) \quad (j = 1, \dots, M). \quad (8)$$

We then solve Eq. (7) (with α_j replacing α for $j = 1, \dots, M$) using an iterative method to reach the steady-state solution. Given the images $\phi_{\alpha_j}^{(k)}$ ($j = 0, \dots, M + 1$) after the k th iteration. We first solve the level-set equation, Eq. (5) with ϕ_{α_j} replacing ϕ with the initial condition $\phi_{\alpha_j}^{(k)}$ ($0 \leq j \leq M + 1$) but only for one time step, followed by the reinitialization (cf. Eq. (6)), and obtain a solution $\phi_{\alpha_j}^*$ which serves as an intermediate image. We then redistribute the intermediate images by linear interpolation to generate new and well-separated images $\phi_{\alpha_j}^{(k+1)}$. More precisely, we set $s_0 = 0$, $s_j = s_{j-1} + \|\phi_{\alpha_j}^* - \phi_{\alpha_{j-1}}^*\|$ ($j = 1, \dots, M + 1$), and $\alpha_j^* = s_j / s_M$ ($j = 0, \dots, M + 1$). For each j ($1 \leq j \leq M$), we find the unique i ($1 \leq i \leq M + 1$)

such that $\alpha_{i-1}^* \leq \alpha_j < \alpha_i^*$. We then calculate $\phi_{\alpha_j}^{(k+1)}$ by the linear interpolation

$$\phi_{\alpha_j}^{(k+1)} = \phi_{\alpha_{i-1}}^* + \frac{\alpha_j - \alpha_{i-1}^*}{\alpha_i^* - \alpha_{i-1}^*} (\phi_{\alpha_i}^* - \phi_{\alpha_{i-1}}^*). \quad (9)$$

All these implementation details are basically summarized in an algorithm in the Supplemental Information of our previous work.¹³ For convenience, we present the algorithm in Section V (APPENDIX).

After we obtain the images of a MEP, we then find an interior image that has the (local) maximum solvation free energy among all the images. This image is an approximation of a saddle point. Note that different initial guesses for the string may lead to different MEPs.

We now apply the climbing string method³⁰ to search for a transition state (i.e., saddle point) along a MEP starting from a known stable equilibrium state represented by the level-set function ϕ_0 . To do so, we choose a level-set function ϕ_1 as an initial guess for a saddle point. As above, we discretize the string into images: $\phi_{\alpha_0}, \phi_{\alpha_1}, \dots, \phi_{\alpha_{M+1}}$. We set the initial end-point images by $\phi_{\alpha_0}^{(0)} = \phi_0$ and $\phi_{\alpha_{M+1}}^{(0)} = \phi_1$, and the initial interior images by Eq. (8). The interior images of the string are evolved by solving the equation (7), one boundary image is fixed at ϕ_0 , and the other boundary image climbs uphill according to a modified direction in which the component of the gradient descent in the tangent direction of the string is reversed.³⁰ The climbing image may jump out of the basin of the state ϕ_0 . This can be checked by evaluating the free energy for each image. If the energies are monotonically increasing, we then keep the entire string; otherwise, we truncate the string up to the first maximum of the energies and keep a part of the images that are monotonically increasing.³⁰ The image is then redistributed to enforce equal arc-length parametrization; cf. Eq. (9). The string converges when the last image approaches a saddle point. After a saddle point is found, we solve the level-set equation (5) with a perturbed saddle point as an initial condition. The perturbation is approximated by using the tangent direction of the string. Thus, the entire MEP can be obtained by relaxation. Our generalized climbing string method is basically summarized in an algorithm presented in the Supplemental Information of our previous work¹³. For convenience, we present the algorithm in Section V (APPENDIX).

III. RESULTS AND ANALYSIS

In our simulations, we use $k_B T$ and Ångström (Å) for the units of energy and length, respectively. Unless specified otherwise, we take $T = 300$ K, $\gamma_0 = 0.1315 k_B T / \text{Å}^2$, $\rho_w = 0.0331 \text{ Å}^{-3}$, $\varepsilon_m = 1$, $\varepsilon_w = 78$, and $\tau = 0.76$ Å. These values are taken from our previous works.^{16,17} The Lorentz–Berthelot mixing rules are applied to determine parameters of the LJ potentials for the water-solute interactions.

A. Two Hydrophobic Plates

We consider the hydration of a nonpolar and hydrophobic model system of two parallel paraffin-like plates, each consisting of 6×6 atoms with the side length about 30 Å. The hydration of such or a similar two-plate system has been extensively investigated with MD simulations and implicit-solvent descriptions.^{16,17,24,32,36–41} For certain plate-plate separations, water molecules between the two plates are metastable, due to the energy penalty arising from less formed hydrogen bonds as opposed to the bulk phase. As a result, these water molecules evaporate and a dewetting (i.e., wet-to-dry) transition occurs. In our previous work,³² we developed a stochastic level-set method that relaxes free energy with the solute-solvent interfacial fluctuations, and studied the dewetting transitions between the two plates. The stochastic level-set method successfully captured the dewetting transition and estimated the activation energy barriers. However, the estimations could be very rough as the rare transition events might not be sufficiently sampled. Here we apply our new approach that couples the variational solvation model and the string method to investigate the dry-wet transitions of such a two-plate system.

To probe the impact of hydrophobicity on the dry-wet transitions, we consider two sets of the LJ parameters for the interaction between water and each solute atom: $\varepsilon = 0.265 k_B T$ and $\sigma = 3.538$ Å (Case 1); $\varepsilon = 0.0485 k_B T$ and $\sigma = 3.538$ Å (Case 2). Thus, Case 2 is relatively more hydrophobic than Case 1. We denote by d (Å) the distance between the two parallel plates, and choose it as the reaction coordinate of the system.

Minimum energy paths. Fig. 2 displays the MEPs connecting the wet and dry states, as well as the solute-solvent interfaces of the wet, dry, and transition state (saddle point) for both Case 1 and Case 2 with the plate-plate distance $d = 12$ Å. As seen from the snapshots

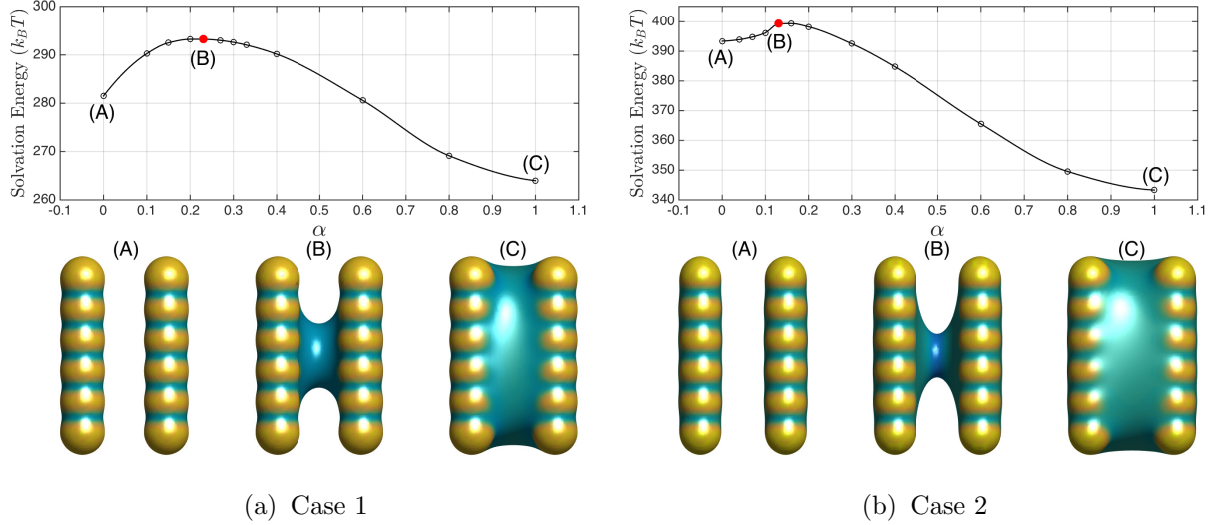


FIG. 2: (Upper part) The minimum energy path connecting the wet state (A) and the dry state (C) for Case 1 (left) and Case 2 (right) with a two-plate separation $d = 12 \text{ \AA}$. Each dot in the curve represents an image of the path (i.e., the string). (Lower part) The corresponding solute-solvent interfaces of the hydration states and the transition state (saddle point (B)). The color indicates the mean curvature of the surface.

(B) for both cases in Fig. 2, the transition state of the dry-wet transition is characterized by a vapor tube spanning two plates. This agrees well with the findings by MD or lattice-gas Monte Carlo (MC) simulations.^{38–40} It is important to observe that the size of the critical vapor tube is larger for Case 1. This is ascribed to the fact that, for a relatively hydrophilic system, a vapor tube of a larger critical size should be nucleated before the evaporation. In addition, the activation energy barrier of the dewetting transition in Case 1 is much larger than that of Case 2, $11.76 k_B T$ vs. $5.95 k_B T$. (The energy barrier for the dewetting, i.e., wet-to-dry, transition is calculated as the difference of the solvation free energy of the transition state (B) and that of the wet state (A). The energy barrier for wetting, i.e., dry-to-wet, transition can be calculated similarly.) This indicates that water molecules are more prone to evaporate in an hydrophobic confinement. Note that the solute-solvent interface of the dry state (C) for Case 1 is slightly tighter than that for Case 2. This is due to a stronger attractive solute-solvent interaction that results from the fact that Case 1 is less hydrophobic.

Energy barriers. We now turn to the dependence of dry-wet transitions on the plate-plate

separations. This requires the calculation of the solvation free energies of all the states and the corresponding activation energy barriers with varying separation distances. To test the performance of our numerical approach, we first do these calculations for Case 1 with both the simplified string method and climbing string method. We find that the solute-solvent interfaces of the transition states computed by the simplified and climbing string methods are nearly the same. (The results are not shown here but can be provided upon request.) This is further confirmed by the data shown in Table I. Both the simplified and climbing string methods predict the same transition states. The surface energy and vdW interaction energy of the transition states have relative discrepancies within 0.1%. The corresponding total solvation free energies have the relative discrepancy within 0.06%. Moreover, the wetting and dewetting energy barriers predicted by the two methods are fairly small, with relative discrepancies to be 0.6% (for wetting) and 1.5% (for dewetting), respectively. These comparisons demonstrate the consistency and effectiveness of our numerical approaches.

—	Simplified String	Climbing String
Surface energy	439.414	439.919
Solute-solvent vdW energy	-146.157	-146.48
Total free energy $G[\Gamma]$	293.257	293.439
Wetting Barrier	29.28	29.46
Dewetting Barrier	11.76	11.94

TABLE I: Solvation free energy and its components of transition states and activation energy barriers (in $k_B T$) for Case 1, predicted by the simplified string method and climbing string method.

We now study the dependence of dry-wet transition energy barriers on the plate-plate separations. First, we note that both dry and wet states exist for a broad range of plate-plate separations $8 \leq d \leq 18 \text{ \AA}$. For this range of separations, Fig. 3 plots the activation energy barrier of the dewetting (i.e., wet-to-dry) transition (B_{wd} , symbols, upper part) and wetting (i.e., dry-to-wet) transition (B_{dw} , symbols, lower part), and the corresponding fitting curves (dotted and solid lines), for both Case 1 and Case 2. (In the figure, “VISM-String” is our model prediction, where VISM stands for variational implicit-solvent model.) For dewetting transitions, the fitted curves of the activation energy barrier are the quadratic polynomials

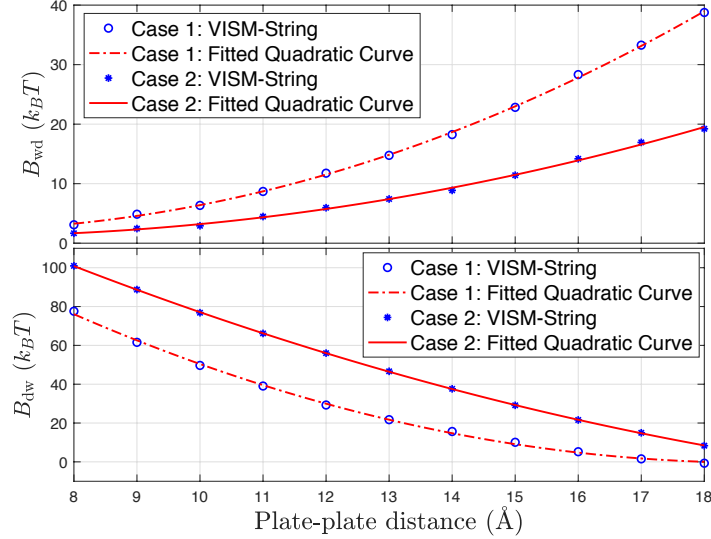


FIG. 3: Activation energy barriers for the dewetting (B_{wd} , upper part) and wetting (B_{dw} , lower part) transitions against the plate-plate separations. (VISM-String is our model prediction. VISM means variational implicit-solvent model.) See Eq. (10)–(13) for the explicit expression of the fitting quadratic curves.

of the plate-plate distance d , given by

$$\text{Case 1: } \quad \beta B_{wd}(d) = 0.251d^2 - 2.954d + 10.848, \quad (10)$$

$$\text{Case 2: } \quad \beta B_{wd}(d) = 0.128d^2 - 1.533d + 5.775, \quad (11)$$

respectively, where $\beta = (k_B T)^{-1}$. For wetting transitions, the fitted curves of the activation energy barrier are the quadratic polynomials of the plate-plate distance d , given by

$$\text{Case 1: } \quad \beta B_{dw}(d) = 0.654d^2 - 24.599d + 231.034, \quad (12)$$

$$\text{Case 2: } \quad \beta B_{dw}(d) = 0.329d^2 - 17.792d + 222.141, \quad (13)$$

respectively.

The quadratic scalings for the dewetting transition agree well with existing predictions by MD simulations.^{39,40} Our hybrid variational approach also predicts a similar quadratic dependence for the wetting transition. We observe that, the energy barrier increases for the dewetting transition but decreases for the wetting transition as the plate-plate separation increases. In addition, the more hydrophobic case (i.e., Case 2) has much lower energy barrier for the dewetting transition and much higher barriers for the wetting transition, respectively.

Case 2 also has a much smaller quadratic coefficients for the dewetting transition than the less hydrophobic Case 1.

We make a final remark on the hydrophobicity and the transition energy barrier. By approximation, we may assume that the critical vapor tube of the transition state is cylindrical; cf. Part (B) of Fig. 2.^{39,40,42,43} As shown in the work,³⁹ the dewetting energy barrier scales quadratically against the plate-plate separation with the quadratic coefficient estimated to be $-\pi\gamma_0/(2\cos\theta)$, where γ_0 is the surface tension and θ is the contact angle of a water droplet on one of the plates. Note that the contact angle is greater than $\pi/2$ for a hydrophobic surface and hence $\cos\theta < 0$. Consequently, the quadratic coefficient should be positive. This is exactly the case for all the quadratic curves we obtained; cf. Eq. (10)–(13). Moreover, Case 2 is more hydrophobic with a larger contact angle θ and thus has a smaller quadratic coefficient for the dewetting transition barrier; cf. Eq. (10) and Eq. (11). Hence, our theory and results are consistent with the macroscopic analysis based on the cylindrical vapor-tube assumption.

B. A Carbon Nanotube

The hydration of nanotubes, nanopores, and transmembrane channels exhibits striking molecular-scale phenomena induced by water.^{4,44–48} For instance, carbon nanotubes (CNTs) in water undergo dry-wet transitions between water-empty dry and water-filled wet states at nanosecond timescale.^{44,45} Dry nanopores with a hydrophobic lining, even not physically occluded, have large permeation barriers to both ions and water molecules, when the diameters of pores are below a critical size.⁴⁸ Dry-wet transitions in nanopores are crucial to such hydrophobic gating that are highly sensitive to the different geometrical length scales of underlying nanopores.^{46,46,47}

Here we apply our variational approach to study the effect of length scales on water evaporation and condensation and the dry-wet transitions in CNTs. We generate two model CNTs by a web-accessible applet⁴⁹ with prescribed chiral indices, (n, m) , that specify the diameter and helicity, and the number of unit cells that determines the length. We denote by D and L the diameter and length of a CNT, respectively; cf. Fig. 4. Specifically, the two CNTs have 8 and 16 unit cells, with lengths about 18.2 Å and 37.6 Å, respectively. The diameters of these two CNTs are both about 20 Å. We label these two CNTs by L8 and L16,

corresponding to their numbers of unit cells, respectively. The parameters of LJ interaction potentials between water and carbon atoms are given by $\varepsilon = 0.1098 k_B T$ and $\sigma = 3.410 \text{ \AA}$.

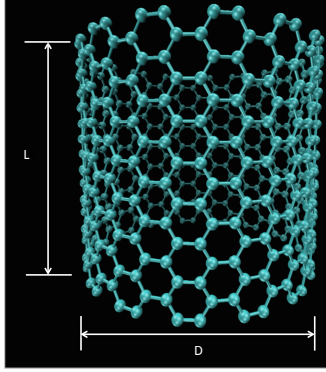


FIG. 4: A schematic plot of a carbon nanotube (CNT). The length and diameter are denoted by L and D , respectively. The chiral indices are given by $(n, m) = (15, 15)$, which correspond to a diameter about 20 \AA . Two cases of CNTs with 8 and 16 unit cells, labeled as L8 and L16, have lengths about 18.2 \AA and 37.6 \AA , respectively.

Fig. 5 displays snapshots of cross sections of solute-solvent interfaces along the dewetting (i.e., wet-to-dry) transition pathways for the CNT L8. There are two types of different paths: (geometrically) symmetric and (geometrically) asymmetric. For the symmetric one, the capillary evaporation starts with the cavitation of a ring-like vapor bubble right in the middle across the nanotube. The bubble subsequently expands and exceeds a certain size that corresponds to the transition state (saddle point); cf. the lower middle plot of Fig. 5. The ring-like vapor region later merges in the middle and spans across the nanotube. As the vapor further grows, the nanotube eventually reaches a dry state. The wetting (i.e., dry-to-wet) transition can be understood by reversing the snapshots. Beginning with water permeation at two ends of the nanotube, the capillary condensation continues with the nucleation of a symmetric hourglass-like liquid bridge along the nanotube at the transition state. The liquid bridge further grows and fills the confinement inside the nanotube, arriving eventually at the wet state.

For an asymmetric path, the capillary evaporation begins with the cavitation of a *meniscus-shaped* vapor bubble adjacent to the inner wall of the nanotube. It grows and reaches the critical size corresponding to the transition state; cf. the upper middle plot of

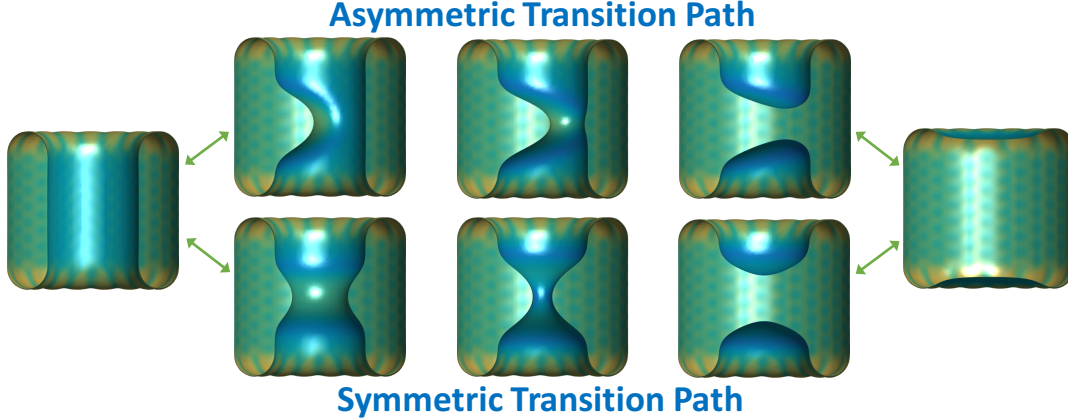


FIG. 5: Cross sections of solute-solvent interfaces along asymmetric (upper part) and symmetric (lower part) transition paths between the wet (left most) and dry (right most) states for the CNT L8. The middle plots depict the solute-solvent interface of the transition states (saddle points).

Fig. 5. After crossing the barrier, the vapor further expands asymmetrically and goes to a dry state. We remark that the asymmetric transition path with a meniscus-shaped transition state configuration agrees perfectly with the MD simulations study,⁵⁰ which reports that the asymmetric path is the most probable path for the evaporation. Note that there can be infinitely many asymmetric paths by the radial symmetry.

The solute-solvent interfaces along the dewetting and wetting transition paths for the CNT L16 are similar, where symmetric and asymmetric paths are also found. (Figures are not shown here.)

We now analyze the corresponding transition energy barriers for these two cases. Fig. 6 shows all the MEPs connecting wet and dry states for both a symmetric path and an asymmetric path for both CNT L8 and L16. Table II lists all the corresponding transition energy barriers. As seen from Fig. 6, the wet state gets destabilized for a longer nanotube, as the favorable energy difference between the wet and dry states decreases. For the CNT L8, the asymmetric path has a slightly lower energy barrier than that of the symmetric one, but energies of the images on symmetric and asymmetric paths are quite different. For the CNT L16, the discrepancy in energy barriers of the symmetric and asymmetric paths is more pronounced, about $2.17 k_B T$, with the asymmetric paths having a lower energy barrier. This indicates that, for both CNTs L8 and L16, the asymmetric paths are more favorable than the symmetric ones. This is consistent with results from MD simulations.⁵⁰

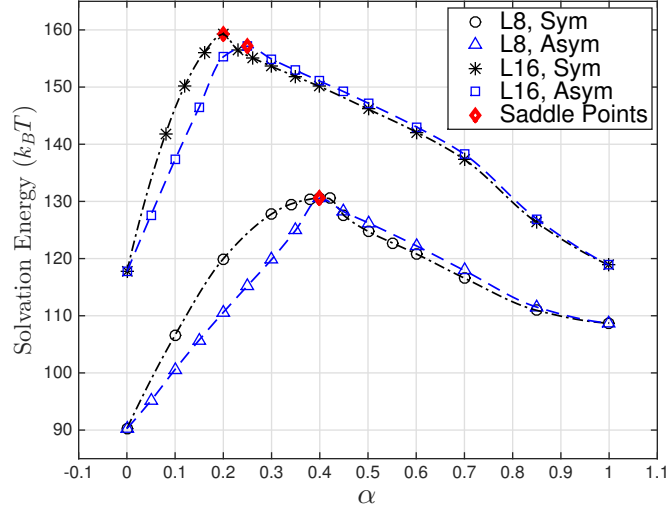


FIG. 6: The MEPs connecting wet ($\alpha = 0$) and dry ($\alpha = 1$) states of the CNTs L8 and L16.

CNT	Dry-to-Wet Transition Barrier ($k_B T$)		Wet-to-Dry Transition Barrier ($k_B T$)	
	Symmetric Path	Asymmetric Path	Symmetric Path	Asymmetric Path
L8	21.92	21.85	40.37	40.30
L16	40.46	38.29	41.61	39.44

TABLE II: Energy barriers for the dry-to-wet and wet-to-dry transitions, both symmetric and asymmetric, for both CNT L8 and L16.

We now discuss the effect of the nanotube length on the dry-wet transitions. For the capillary evaporation, the energy barrier does not change much as the nanotube becomes longer. This is because the energy cost of the cavitation of the vapor bubble over a certain size does not increase much for a longer nanotube. However, the energy barrier of capillary condensation increases significantly from $21.85 k_B T$ to $38.29 k_B T$ for the asymmetric path and from $21.92 k_B T$ to $40.46 k_B T$ for the symmetric case, respectively, as the length of the nanotube increases. This can be explained by the observation that the energy cost of the nucleation of the liquid bridge over a certain size along the nanotube is much larger for a longer nanotube. According to the Arrhenius law, the condensation transition rate is exponentially smaller for the CNT L16. Our results demonstrate that, in contrast to evaporation, the condensation transition is relatively more sensitive to the length of the

nanotube.

C. Cucurbit[7]uril

The synthetic Cucurbit[7]uril (CB[7]) host molecule has various potential applications, such as molecular machines and drug transport,⁵¹⁻⁵³ partially due to its ultra-high binding affinity with aromatic guests or metal complexes.^{52,54,55} The special structure of this ring-shaped, charged molecule makes it hard for water molecules to form a stable H-bond network inside its hydrophobic cavity with limited space. Rather, water molecules fluctuate, and the cavity undergoes dry and wet transitions,^{12,56} providing increased opportunities for an approaching guest molecule or ion to replace water molecules in the cavity, and hence significantly enhance the binding affinity.⁵⁴

Previously, we applied our level-set variational implicit solvation model with the CFA of electrostatics to CB[7], and captured efficiently its different dry and wet states.^{17,22,23} We found that the electrostatic interactions contribute significantly to the stability of the dry and wet states: the hydration free energy of the wet state is higher than that of the dry state without the electrostatics, but is lower than that of the dry state if the electrostatics is included. MD simulations have confirmed our results.^{22,56} In Zhou *et al.*²², we also studied the binding of the host-guest system CB[7]-B2, and found that the accuracy of the CFA approximation of electrostatic energy and hence the total free-energy estimation was sensitive to the location of dielectric boundary and the solute conformation. A loose boundary produced a much better free-energy estimation than a tight one. In addition, a rigid-body approximation of the host-guest binding could lead to a large error in the binding affinity.

It is known that the replacement of water molecules in the hydrophobic cavity of CB[7] contributes significantly to the binding affinity of a guest molecule to the CB[7] host. Here we study the dry-wet transition paths of CB[7], and the role of electrostatics to such transitions. We first consider a noncharged version of CB[7] by turning off manually all the solute charges of CB[7]. For such a noncharged CB[7], the dry state is more favorable than the wet state.^{17,22,56} Our level-set string method captures two different MEPs: (geometrically) symmetric and (geometrically) asymmetric transition pathways; cf. Fig. 7. The plots of interfacial structures from left to right in Fig. 7 correspond to a dewetting (i.e., wet-to-dry) transition, or capillary evaporation. For the asymmetric transition path, the evaporation

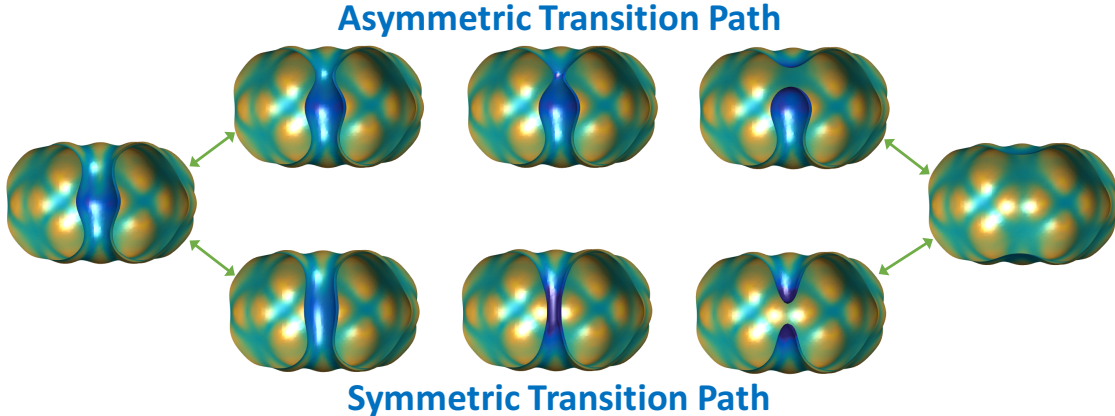


FIG. 7: Cross sections (perpendicular to the plane of the circular ring) of solute-solvent interfaces along asymmetric (upper part) and symmetric (lower part) transition paths between wet (left most) and dry (right most) states of a noncharged CB[7]. The middle plots depict the solute-solvent interfaces of transition states (saddle points).

starts with the cavitation of a ring-like bubble in the region close to one of the two mouths of the cavity. After the bubble exceeds a certain critical size corresponding to the transition state, the ring-like bubble merges into a connected one at a mouth of CB[7] and water molecules further evaporate from the cavity through the other mouth. For the symmetric case, the evaporation begins with the cavitation of a ring-like bubble in the middle of the cavity. Then the bubble further grows into a connected one in the middle of the cavity. After crossing the transition state, water molecules further evaporate symmetrically through two mouths of the cavity. The plots from right to left in Fig. 7 correspond to the wetting (i.e., dry-to-wet) transition of capillary condensation, which has symmetric and asymmetric transition pathways as well. In the condensation, the water molecules permeate into the cavity region through two mouths, and further connect and span the cavity region at the transition state. After crossing the associated energy barrier, the water molecules continue to fill in the cavity, reaching eventually the wet state.

For the case with electrostatics, the wet state is more favorable, and the solute-solvent interface for a dry and wet state is much tighter than that of the non-charged case.^{17,22,56} Our method captures again two transition paths connecting the wet and dry states; cf. Fig. 8. Note that the critical size of the cavitated bubble at the transition state is larger for both symmetric and asymmetric transition paths, resulting from the attractive electrostatic

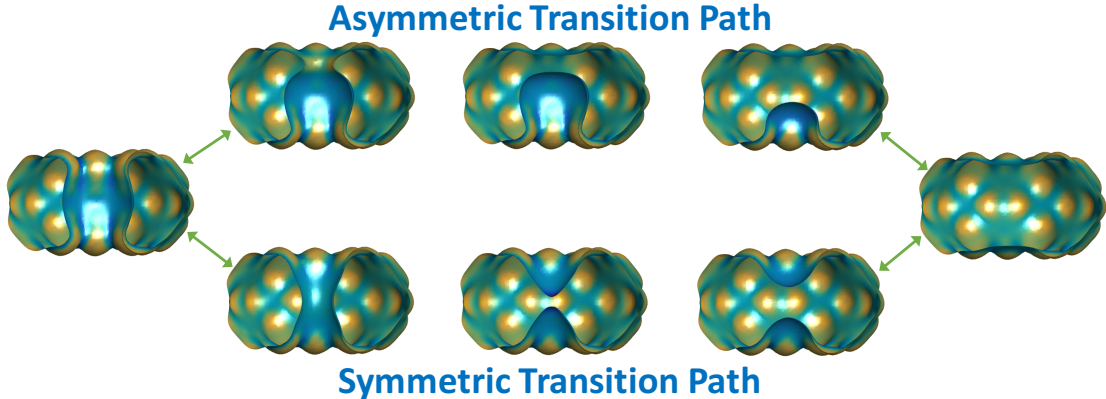


FIG. 8: Cross sections of solute-solvent interfaces along asymmetric and symmetric transition paths between wet (Left) and dry (Right) states of a charged Cucurbit[7]uril. The middle plots depict the solute-solvent interfaces of transition states (saddle points).

interactions between charged solute atoms and water. In contrast to the non-charged case, the permeated water into the cavity from two mouths does not have to connect at the transition states for both symmetric and asymmetric condensation pathways.

Fig. 9 shows the MEPs connecting wet ($\alpha = 0$) and dry ($\alpha = 1$) states, corresponding to symmetric and asymmetric transition paths. We see clearly that the dry state has lower solvation free energies for the noncharged case but the wet state is energetically more favor-

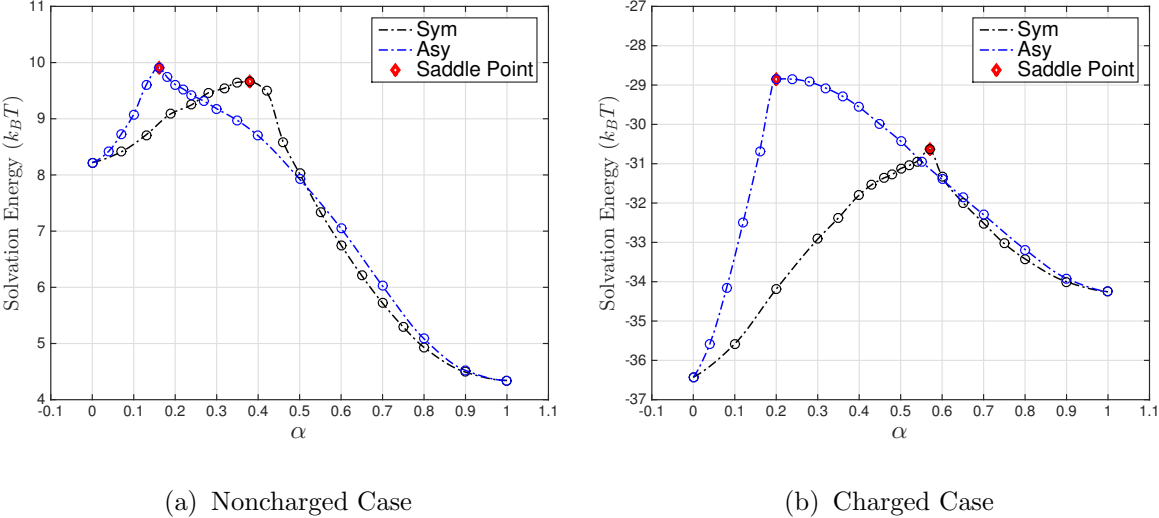


FIG. 9: Multiple MEPs connecting the wet ($\alpha = 0$) and dry ($\alpha = 1$) states of a charged or noncharged CB[7]. The symmetric and asymmetric transition paths are marked by “Sym” and “Asy”, respectively.

able for the charged case. For the noncharged case, the symmetric transition path involves a slightly lower activation energy barrier. Table III shows that the energy barriers for the dewetting transition are $1.44 k_B T$ for the symmetric path and $1.69 k_B T$ for the asymmetric path, respectively. In wetting transitions, the symmetric path again has a lower barrier, 5.32 vs. $5.57 k_B T$. We then consider the charged case. Since the wet state is more favorable, wetting energy barriers decrease and become lower than dewetting energy barriers. The dewetting energy barriers of the symmetric and asymmetric path increase to $5.80 k_B T$ and $7.59 k_B T$, respectively. This again can be explained by the electrostatic attractions between water and charged solute atoms. Also, the symmetric wetting path has a lower energy barrier, 3.62 vs. $5.42 k_B T$. Therefore, the discrepancy in activation energy barriers of symmetric and asymmetric paths is magnified by the electrostatic interactions.

—	Noncharged	Charged
Dewetting (Sym)	1.44	5.80
Dewetting (Asy)	1.69	7.59
Wetting (Sym)	5.32	3.62
Wetting (Asy)	5.57	5.42

TABLE III: Activation energy barriers (in $k_B T$) of symmetric and asymmetric transition paths for the charged and noncharged cases.

IV. CONCLUSIONS

Dewetting and wetting transitions are ubiquitous in molecular processes in water, and pathways of such transitions encode abundant thermodynamic and kinetic information. Efficient and detailed predictions of such pathways are therefore essential to quantitative and applicable understanding of complex molecular dynamics in materials and biological systems. Here, we have developed a hybrid, mesoscale, variational modeling framework, numerically implemented such a model, and studied in quantitative details the dewetting and wetting transition paths for several molecular systems of practical interest.

Our approach combines a mesoscale variational solvation model for finding multiple, stable, equilibrium dry and wet solvation states, and generalized string methods for finding

different transition paths connecting those states. With our implicit-solvent model, we can determine a stable equilibrium solute-solvent interface (i.e., dielectric boundary) and the corresponding solvation free energy by minimizing a free-energy functional of all possible solute-solvent interfaces enclosing all the solute atoms. The string method is generalized here for our variational free-energy landscape. An image of a string is a surface here instead of a point in a Euclidean space. We have implemented a level-set numerical method to minimize our solvation free-energy functional of interfaces and to find MEPs with three-dimensional geometry. Tests of our implementation show consistent performance of our methods (cf. Subsection III A). Our computations usually take minutes to hours, rather fast compared to corresponding explicit-water MD simulations.

We applied our modeling framework and numerical methods to study the transition paths of a model system of two hydrophobic plates, and a carbon nanotube and a synthetic host molecule CB[7] that are of much interest in applications. For each of these systems, we have obtained the dry and wet solvation states, transition paths, transition states, and the energy barriers. Here are highlights of our results:

- (1) Details of the dewetting and wetting transitions depend sensitively on the length scales, geometry, hydrophobicity, and electrostatic interactions of an underlying molecular system. For instance, the separation distance of the two-plate and the length of the CNT all play crucial roles in the transition paths.
- (2) We find multiple transition paths, geometrically symmetric and asymmetric, in the hydration of CNT (both cases) and in CB[7]. By radial symmetry, there can be infinitely many asymmetric paths. As the geometry and topology of many biological molecules are far more complex, it is reasonable to expect that multiple transition paths exist in general solvation systems.
- (3) Energy barriers in wetting and dewetting transitions are rather different. For the two-plate system, the energy barrier depends on the plate-plate separation increasingly for the dewetting transition but decreasingly for the wetting transition. With the electrostatics, the energy barrier in the dewetting transition is much higher than the wetting transition in the hydration of charged CB[7].
- (4) Our efficient mesoscale theory and methods can capture details of wetting and dewetting transition paths, and our results agree well with MD simulations. In particular, for the two-plate system, the quadratic dependence of the transition energy barrier on

the plate-plate separation distance is in very good quantitative agreement with existing MD simulations.

We now discuss several issues and possible further improvements of our approach. First, the CFA of electrostatics is efficient but it does not include the ionic charge effect. It also depends sensitively on the location of dielectric boundary, leading possibly to a poor ensemble average of electrostatic free energy from only a few equilibrium states. Therefore, for some molecular systems, large errors can occur in electrostatic free-energy estimation. The generalized Born (GB) model^{18,57} is computationally efficient and is also able to include the ionic screening effect with some parameter adjustment. But the GB model is based on Born radii which determine a dielectric boundary from a collection of spheres. Our solvation model, however, relies crucially on the variation of a dielectric boundary. A possible way is to include the ionic screen effect in a generalized CFA of electrostatics using the Yukawa (or Debye–Hückel) potentials associated with solute atoms as done in the GB model. We can also use the Poisson–Boltzmann (PB) model for the electrostatics.^{17,58–61} But this will be computationally costly, as one needs to solve the PB equation in each iteration step of the free-energy minimization. One can combine the PB and CFA by using the CFA in most of the iteration steps and then using the PB in the last few steps. A potential issue is that the CFA may change the energy landscape and hence may mislead the VISM minimization path. Other continuum models of electrostatics, such as Gaussian-based dielectric model,⁶² may be of interest and should be considered.

Second, for relatively simple solvation systems, we can capture different dry and wet solvation states by constructing different initial solute-solvent interfaces and then minimizing our solvation free-energy functional with a steepest descent method. In general, we should include the solute mechanical interactions³⁴ and sample the conformation spaces to find different solvation states.

Third, we have been able to capture transition paths with simple reaction coordinates. For more complex molecular systems, where the dry and wet transitions may depend on collective motions of solute atoms. It will be then necessary to introduce collective variables such as solute atomic positions as reaction coordinates, in addition to the solvent effects implicitly described by the level-set function.

Fourth, MEPs defined in the string method that we have used represent most probable transition paths, according to the large deviation theory.³⁵ However, there in general exist an

ensemble of transition paths connecting different metastable states. The finite-temperature string method^{27,63} may be more effective in identifying the isocommittor surfaces in the region of configuration space where the most probable transition paths are concentrated. It is our next step to combine such a finite-temperature string method with our variational solvation model to investigate transitions of biomolecular solvation states.

Finally, our computations of molecular equilibrium properties, such as dry and wet states, the transition paths, and the transition states and energy barriers, not only describe the thermodynamic stabilities but also provide data for estimating kinetic rates using Brownian dynamics simulation or Fokker–Planck equation modeling.¹³ It will be interesting to apply such a systematic approach to more complex molecular processes, particularly protein folding and protein-ligand binding and unbinding.

V. APPENDIX

Algorithm of a generalized simplified string method.

Step 1. Input all the parameters γ_0 , τ , ρ_w , N , and \mathbf{x}_i , Q_i , σ_i , and ε_i ($i = 1, \dots, N$). Input a computational box and a spatial discretization mesh. Input the level-set functions ϕ_0 and ϕ_1 of two stable equilibrium states as the two end images of a string. Input M , the number of (interior) images in the string, the parameters α_j ($j = 0, 1, \dots, M + 1$) for the string images with $0 = \alpha_0 < \alpha_1 < \dots < \alpha_{M+1} = 1$, and the initial interior image level-set functions $\phi_j^{(0)}$ ($j = 1, \dots, M$); cf. Eq. (8). Set the iteration counter $k = 0$.

Step 2. Given the interior images $\phi_{\alpha_j}^{(k)}$ ($j = 1, \dots, M$). For each j ($1 \leq j \leq M$), solve the level-set equation (5) with ϕ_{α_j} replacing ϕ using the initial solution $\phi_{\alpha_j}^{(k)}$ for one time step to obtain the image $\bar{\phi}_{\alpha_j}$. Compute the image $\phi_{\alpha_j}^*$ by solving the reinitialization equation (6) with $\bar{\phi}_{\alpha_j}$ as the initial solution.

Step 3. Compute the arc lengths $s_0 = 0$ and $s_j = s_{j-1} + \|\phi_{\alpha_j}^* - \phi_{\alpha_{j-1}}^*\|$ ($j = 1, \dots, M + 1$) and the parameters $\alpha_j^* = s_j/s_M$ ($j = 0, 1, \dots, M + 1$). Generate the images $\phi_{\alpha_j}^{(k+1)}$ ($j = 1, \dots, M$) by Eq. (9).

Step 4. Check the stopping criteria. If failed, set $k := k + 1$ and go to Step 2.

Algorithm for a generalized climbing string method.

Step 1. Input all the parameters γ_0 , τ , ρ_w , N , and \mathbf{x}_i , Q_i , σ_i , and ε_i ($i = 1, \dots, N$). Input a

computational box and a spatial discretization mesh. Input a level-set function ϕ_0 that represents a stable equilibrium state and a level-set function ϕ_1 as a rough initial guess of a saddle point near ϕ_0 . Input M , with $M + 2$ the number of images in the string, the parameters $\{\alpha_j\}_{j=0}^{M+1}$ for the string images with $0 = \alpha_0 < \alpha_1 < \dots < \alpha_{M+1} = 1$, and the initial interior image level-set functions $\{\phi_{\alpha_j}^{(0)}\}_{j=1}^M$. Set the iteration counter $k = 0$.

Step 2. Given the images $\phi_{\alpha_j}^{(k)}$ ($j = 1, \dots, M + 1$). For each j ($1 \leq j \leq M + 1$), solve the level-set equation (5) using the initial solution $\phi_{\alpha_j}^{(k)}$ for one time step to obtain an image $\bar{\phi}_j$. Solve the reinitialization equation (6) using the initial solution $\bar{\phi}_j$ for one time step to obtain an image ϕ_j^* .

Step 3. Update the last image by reflection

$$\phi_{\alpha_{M+1}}^{(k+1)} = \phi_{M+1}^* - 2 \left\langle \phi_{M+1}^* - \phi_{\alpha_{M+1}}^{(k)}, \hat{\tau}_{M+1} \right\rangle \hat{\tau}_{M+1} \quad \text{with} \quad \hat{\tau}_{M+1} = \frac{\phi_{\alpha_{M+1}}^{(k)} - \phi_{\alpha_M}^{(k)}}{\|\phi_{\alpha_{M+1}}^{(k)} - \phi_{\alpha_M}^{(k)}\|},$$

where $\langle \cdot, \cdot \rangle$ denotes the $L^2(\Omega)$ -inner product.

Step 4. If needed, truncate the string to ensure that the images in the string have monotonically increasing energies.

Step 5. Compute the arc lengths $s_0 = 0$ and $s_j = s_{j-1} + \|\phi_{\alpha_j}^* - \phi_{\alpha_{j-1}}^*\|$ ($j = 1, \dots, M + 1$), and set $\alpha_j^* = s_j/s_M$ ($j = 0, 1, \dots, M + 1$). Update the other interior images to obtain $\phi_{\alpha_j}^{(k+1)}$ ($j = 1, \dots, M$) by Eq. (9).

Step 6. Check the stopping criteria. If failed, set $k := k + 1$ and go to Step 2.

Acknowledgments. SZ was supported by National Natural Science Foundation of China (NNSFC) through grant No. 21773165, Natural Science Foundation of Jiangsu Province, China, through grant No. BK20200098, and National Key R&D Program of China through grant 2018YFB0204404. YZ was supported by NNSFC through grant No. 11871365 and Natural Science Foundation of Jiangsu Higher Education Institutions of China through grant No. 19KJB110020. LTC and BL were supported in part by the US National Science Foundation through grant DMS-1913144. BL was also supported in part by the US National Institutes of Health through grant R01GM132106.

Conflicts of interest. The authors have no conflicts to disclose.

Data Availability. The data that support the findings of this study are available from the

corresponding author upon reasonable request.

- ¹ Levy, Y.; Onuchic, J. Water mediation in protein folding and molecular recognition. *Ann. Rev. Biophys. Biomol. Struct.* **2006**, *35*, 389–415.
- ² Rasaiah, J. C.; Garde, S.; Hummer, G. Water in nonpolar confinement: From nanotubes to proteins and beyond. *Annu. Rev. Phys. Chem.* **2008**, *59*, 713–740.
- ³ Baron, R.; McCammon, J. A. Molecular recognition and ligand association. *Annu. Rev. Phys. Chem.* **2013**, *64*, 151–175.
- ⁴ Lynch, C. I.; Rao, S.; Sansom, M. S. P. Water in nanopores and biological channels: A molecular simulation perspective. *Chem. Rev.* **2020**, *120*, 10298–10335.
- ⁵ Hummer, G.; Garde, S.; Garcia, S.; Pratt, L. R. New perspectives on hydrophobic effects. *Chem. Phys.* **2000**, *258*, 349–370.
- ⁶ Chandler, D. Interfaces and the driving force of hydrophobic assembly. *Nature* **2005**, *437*, 640–647.
- ⁷ Berne, B. J.; Weeks, J. D.; Zhou, R. Dewetting and hydrophobic interaction in physical and biological systems. *Annu. Rev. Phys. Chem.* **2009**, *60*, 85–103.
- ⁸ Dill, K. A. Dominant forces in protein folding. *Biochem.* **1990**, *29*, 7133–7155.
- ⁹ Liu, P.; Huang, X.; Zhou, R.; Berne, B. J. Observation of dewetting transition in the collapse of the melittin tetramer. *Nature* **2005**, *437*, 159–162.
- ¹⁰ Wang, L.; Berne, B. J.; Friesner, R. A. Ligand binding to protein-binding pockets with wet and dry regions. *Proc. Natl. Acad. Sci. USA* **2011**, *108*, 1326–1330.
- ¹¹ Mondal, J.; Morrone, J.; Berne, B. J. How hydrophobic drying forces impact the kinetics of molecular recognition. *Proc. Natl. Acad. Sci., USA* **2013**, *110*, 13277–13282.
- ¹² Setny, P.; Baron, R.; Kekenes-Huskey, P. M.; McCammon, J. A.; Dzubiella, J. Solvent fluctuations in hydrophobic cavity-ligand binding kinetics. *Proc. Natl. Acad. Sci., USA* **2013**, *110*, 1197–1202.
- ¹³ Zhou, S.; Weiß, R. G.; Cheng, L.-T.; Dzubiella, J.; McCammon, J. A.; Li, B. Variational implicit-solvent predictions of the dry–wet transition pathways for ligand–receptor binding and unbinding kinetics. *Proc. Natl. Acad. Sci. U.S.A.* **2019**, *116*, 14989–14994.
- ¹⁴ Dzubiella, J.; Swanson, J. M. J.; McCammon, J. A. Coupling hydrophobicity, dispersion, and

- electrostatics in continuum solvent models. *Phys. Rev. Lett.* **2006**, *96*, 087802.
- ¹⁵ Dzubiella, J.; Swanson, J. M. J.; McCammon, J. A. Coupling nonpolar and polar solvation free energies in implicit solvent models. *J. Chem. Phys.* **2006**, *124*, 084905.
- ¹⁶ Wang, Z.; Che, J.; Cheng, L.-T.; Dzubiella, J.; Li, B.; McCammon, J. A. Level-set variational implicit solvation with the Coulomb-field Approximation. *J. Chem. Theory Comput.* **2012**, *8*, 386–397.
- ¹⁷ Zhou, S.; Cheng, L.-T.; Dzubiella, J.; Li, B.; McCammon, J. A. Variational implicit solvation with Poisson–Boltzmann theory. *J. Chem. Theory Comput.* **2014**, *10*, 1454–1467.
- ¹⁸ Bashford, D.; Case, D. A. Generalized Born models of macromolecular solvation effects. *Ann. Rev. Phys. Chem.* **2000**, *51*, 129–152.
- ¹⁹ Borgis, D.; Levy, N.; Marchi, M. Computing the electrostatic free-energy of complex molecules: The variational Coulomb field approximation. **2003**, *119*, 3516.
- ²⁰ Cheng, H. B.; Cheng, L.-T.; Li, B. Yukawa-field approximation of electrostatic free energy and dielectric boundary force. *Nonlinearity* **2011**, *24*, 3215–3236.
- ²¹ Guo, Z.; Li, B.; Dzubiella, J.; Cheng, L.-T.; McCammon, J. A.; Che, J. Evaluation of hydration free energy by the level-set variational implicit-solvent model with the Coulomb-Field approximation. *J. Chem. Theory Comput.* **2013**, *9*, 1778–1787.
- ²² Zhou, S.; Rogers, K. E.; de Oliveira, C. A. F.; Baron, R.; Cheng, L.-T.; Dzubiella, J.; Li, B.; McCammon, J. A. Variational implicit-solvent modeling of host-guest binding: A case study on Cucurbit[7]uril. *J. Chem. Theory Comput.* **2013**, *9*, 4195–4204.
- ²³ Zhou, S.; Cheng, L.; Sun, H.; Che, J.; Dzubiella, J.; Li, B.; McCammon, J. A. LS-VISM: A software package for analysis of biomolecular solvation. *J. Comput. Chem.* **2015**, *36*, 1047–1059.
- ²⁴ Cheng, L.-T.; Dzubiella, J.; McCammon, J. A.; Li, B. Application of the level-set method to the implicit solvation of nonpolar molecules. *J. Chem. Phys.* **2007**, *127*, 084503.
- ²⁵ Cheng, L.-T.; Li, B.; Wang, Z. Level-set minimization of potential controlled Hadwiger valuations for molecular solvation. *J. Comput. Phys.* **2010**, *229*, 8497–8510.
- ²⁶ E, W.; Ren, W.; Vanden-Eijnden, E. String method for the study of rare events. *Phys. Rev. B* **2002**, *66*, 052301.
- ²⁷ E, W.; Ren, W.; Vanden-Eijnden, E. Finite temperature string method for the study of rare events. *J. Phys. Chem. B* **2005**, *109*, 6688–6693.
- ²⁸ E, W.; Ren, W.; Vanden-Eijnden, E. Simplified and improved string method for computing the

- minimum energy paths in barrier-crossing events. *J. Chem. Phys.* **2007**, *126*, 164103.
- ²⁹ E, W.; Vanden-Eijnden, E. Transition-path theory and path-finding algorithms for the study of rare events. *Ann. Rev. Phys. Chem.* **2010**, *61*, 391–420.
- ³⁰ Ren, W.; Vanden-Eijnden, E. A climbing string method for saddle point search. *J. Chem. Phys.* **2013**, *138*, 134105.
- ³¹ Zhang, Z.; Ricci, C. G.; Fan, C.; Cheng, L.-T.; Li, B.; McCammon, J. A. Coupling Monte Carlo, variational implicit solvation, and binary level-set for simulations of biomolecular binding. *J. Chem. Theory Comput.* **2021**, *17*, 2465–2478.
- ³² Zhou, S.; Sun, H.; Cheng, L.-T.; Dzubiella, J.; Li, B.; McCammon, J. A. Stochastic level-set variational implicit-solvent approach to solute-solvent interfacial fluctuations. *J. Chem. Phys.* **2016**, *145*, 054114.
- ³³ Tolman, R. C. The effect of droplet size on surface tension. *J. Chem. Phys.* **1949**, *17*, 333–337.
- ³⁴ Cheng, L.-T.; Xie, Y.; Dzubiella, J.; McCammon, J. A.; Che, J.; Li, B. Coupling the level-set method with molecular mechanics for variational implicit solvation of nonpolar molecules. *J. Chem. Theory Comput.* **2009**, *5*, 257–266.
- ³⁵ Freidlin, M. I.; Wentzell, A. D. *Random Perturbations of Dynamical Systems*; Springer, New York, 1998.
- ³⁶ Koishi, T.; Yoo, S.; Yasuoka, K.; Zeng, X. C.; Narumi, T.; Susukita, R.; Kawai, A.; Furusawa, H.; Suenaga, A.; Okimoto, N.; Futatsugi, N.; Ebisuzaki, T. Nanoscale hydrophobic interaction and nanobubble nucleation. *Phys. Rev. Lett.* **2004**, *93*, 185701.
- ³⁷ Luzar, A. Activation barrier scaling for the spontaneous evaporation of confined water. *J. Phys. Chem. B* **2004**, *108*, 19859–19866.
- ³⁸ Choudhury, N.; Pettitt, B. M. On the mechanism of hydrophobic association of nanoscopic solutes. *J. Am. Chem. Soc.* **2005**, *127*, 3556–3567.
- ³⁹ Sharma, S.; Debenedetti, P. G. Free energy barriers to evaporation of water in hydrophobic confinement. *J. Phys. Chem. B* **2012**, *116*, 13282–13289.
- ⁴⁰ Sharma, S.; Debenedetti, P. G. Evaporation rate of water in hydrophobic confinement. *Proc. Natl. Acad. Sci., USA* **2012**, *109*, 4365–4370.
- ⁴¹ Hua, L.; Zangi, R.; Berne, B. J. Hydrophobic interactions and dewetting between plates with hydrophobic and hydrophilic domains. *J. Phys. Chem. C* **2009**, *113*, 5244–5253.
- ⁴² Leung, K.; Luzar, A.; Bratko, D. Dynamics of capillary drying in water. *Phys. Rev. Lett.* **2003**,

- 90, 065502.
- ⁴³ Remsing, R. C.; Xi, E.; Vembanur, S.; Sharma, S.; Debenedetti, P. G.; Garde, S.; Patel, A. J. Pathways to dewetting in hydrophobic confinement. *Proc. Natl. Acad. Sci. USA* **2015**, *112*, 8181–8186.
- ⁴⁴ Hummer, G.; Rasaiah, J. C.; Nowortya, J. P. Water conduction through the hydrophobic channel of a carbon nanotube. *Nature* **2001**, *414*, 188.
- ⁴⁵ Waghe, A.; Rasaiah, J. C.; Hummer, G. Filling and emptying kinetics of carbon nanotubes in water. *J. Chem. Phys.* **2002**, *117*, 10789.
- ⁴⁶ Beckstein, O.; Biggin, P. C.; Sansom, M. S. P. A hydrophobic gating mechanism for nanopores. *J. Phys. Chem. B* **2001**, *105*, 12902.
- ⁴⁷ Beckstein, O.; Sansom, M. S. P. Liquid–vapor oscillations of water in hydrophobic nanopores. *Proc. Natl. Acad. Sci., USA* **2003**, *100*, 7063–7068.
- ⁴⁸ Beckstein, O.; Tai, K.; Sansom, M. S. P. Not ions alone: Barriers to ion permeation in nanopores and channels. *J. Am. Chem. Soc.* **2004**, *126*, 14694–14695.
- ⁴⁹ <http://www.nanotube.msu.edu/tubeASP/>.
- ⁵⁰ Tinti, A.; Giacomello, A.; Grosu, Y.; Casciola, C. M. Intrusion and extrusion of water in hydrophobic nanopores. *Proc. Natl. Acad. Sci., USA* **2017**, *114*, E10266–10273.
- ⁵¹ Lagona, J.; Mukhopadhyay, P.; Chakrabarti, S.; Isaacs, L. The Cucurbit[n]uril family. *Angew. Chem., Int. Ed. Engl.* **2005**, *44*, 4844–4870.
- ⁵² Liu, S.; Ruspic, C.; Mukhopadhyay, P.; Chakrabarti, S.; Zavalij, P. Y.; Isaacs, I. The Cucurbit[n]uril family: Prime components for self-sorting systems. *J. Am. Chem. Soc.* **2005**, *127*, 15959–15967.
- ⁵³ Assaf, K. I.; Nau, W. M. Cucurbiturils: from synthesis to high-affinity binding and catalysis. *Chem. Soc. Rev.* **2015**, *44*, 394–418.
- ⁵⁴ Rekharsky, M. V.; Mori, T.; Yang, C.; Ko, Y. H.; Selvapalam, N.; Kim, H.; Sobransingh, D.; Kaifer, A. E.; Liu, S.; Isaacs, L.; Chen, W.; Moghaddam, S.; Gilson, M. K.; Kim, K.; Inoue, Y. A synthetic host-guest system achieves Avidin-Biotin affinity by overcoming enthalpy-entropy compensation. *Proc. Natl. Acad. Sci. USA* **2007**, *104*, 20737–20742.
- ⁵⁵ Moghaddam, S.; Inoue, Y.; Gilson, M. K. Host-guest complexes with protein-ligand-like affinities: Computational analysis and design. *J. Am. Chem. Soc.* **2009**, *131*, 4012–4021.
- ⁵⁶ Rogers, K. E.; Ortiz-Sánchez, J. M.; Baron, R.; Fajer, M.; de Oliveira, C. A. F.; McCam-

- mon, J. A. On the role of dewetting transitions in host-guest binding free energy calculations. *J. Chem. Theory Comput.* **2013**, *9*, 46–53.
- ⁵⁷ Onufriev, A. V.; Case, D. A. Generalized Born implicit solvent models for biomolecules. *Annu. Rev. Biophys.* **2019**, *48*, 275–296.
- ⁵⁸ Davis, M. E.; McCammon, J. A. Electrostatics in biomolecular structure and dynamics. *Chem. Rev.* **1990**, *90*, 509–521.
- ⁵⁹ Sharp, K. A.; Honig, B. Electrostatic interactions in macromolecules: Theory and applications. *Annu. Rev. Biophys. Chem.* **1990**, *19*, 301–332.
- ⁶⁰ Che, J.; Dzubiella, J.; Li, B.; McCammon, J. A. Electrostatic free energy and its variations in implicit solvent models. *J. Phys. Chem. B* **2008**, *112*, 3058–3069.
- ⁶¹ Cai, Q.; Wang, J.; Hsieh, M. J.; Ye, X.; Luo, R. Poisson–Boltzmann Implicit Solvation Models. *Annu. Rep. Comput. Chem.* **2012**, *8*, 149–162.
- ⁶² Chakravorty, A.; Panday, S.; Pahari, S.; Zhao, S.; Alexov, E. Capturing the effects of explicit waters in implicit electrostatics modeling: Qualitative justification of Gaussian-based dielectric models in DelPhi. *J. Chem. Inf. Model.* **2020**, *60*, 2229–2246.
- ⁶³ Ren, W.; Vanden-Eijnden, E.; Maragakis, P.; E, W. Transition pathways in complex systems: Application of the finite-temperature string method to the alanine dipeptide. *J. Chem. Phys.* **2005**, *123*, 134109.